

RESEARCH ARTICLE | NOVEMBER 06 2024

Ensemble Monte Carlo transport studies of zinc-blende cuprous halides

Min Hyeok Kim  ; Byoung Don Kong  *J. Appl. Phys.* 136, 175704 (2024)<https://doi.org/10.1063/5.0236614>

Articles You May Be Interested In

The Lattice Energies of the Cuprous Halides

J. Chem. Phys. (September 1933)

Temperature dependence of NMR chemical shifts in cuprous halides

J. Chem. Phys. (April 1978)

Accuracy trade-off between one-electron and excitonic spectra of cuprous halides in first-principles calculations

J. Chem. Phys. (April 2021)Nanotechnology &
Materials ScienceOptics &
PhotonicsImpedance
AnalysisScanning Probe
Microscopy

Sensors

Failure Analysis &
Semiconductors

Unlock the Full Spectrum. From DC to 8.5 GHz.

Your Application. Measured.

[Find out more](#)

Ensemble Monte Carlo transport studies of zinc-blende cuprous halides

Cite as: J. Appl. Phys. **136**, 175704 (2024); doi: [10.1063/5.0236614](https://doi.org/10.1063/5.0236614)

Submitted: 1 September 2024 · Accepted: 22 October 2024 ·

Published Online: 6 November 2024



Min Hyeok Kim  and Byoung Don Kong 

AFFILIATIONS

Department of Electrical Engineering, Pohang University of Science and Technology (POSTECH), Pohang 37673, Republic of Korea

^{a)}Author to whom correspondence should be addressed: bdkong@postech.ac.kr

ABSTRACT

We present a comprehensive theoretical analysis of intrinsic high-field transport in cuprous halides: CuCl, CuBr, and CuI. Ensemble Monte Carlo transport simulations were performed based on analytical approximations of the *multi-valley* and *three-band* electronic structure model. The deformation potentials, extracted from carrier-phonon interaction matrix elements calculated via the Wannier function approach, were employed to determine scattering rates. Our detailed analysis uncovers intriguing transport characteristics based on the complex valence band structures, resulting from spin-orbit coupling and band inversion. Remarkably, the hole mobility in CuI was exceptionally high, reaching up to $193 \text{ cm}^2/\text{V s}$, while CuCl exhibited unusual temperature dependencies in hole transport. Additionally, the electron mobility in CuI was found to be $254 \text{ cm}^2/\text{V s}$, indicating a minimal disparity between carrier mobilities, which is advantageous for optoelectronic applications.

© 2024 Author(s). All article content, except where otherwise noted, is licensed under a Creative Commons Attribution-NonCommercial 4.0 International (CC BY-NC) license (<https://creativecommons.org/licenses/by-nc/4.0/>). <https://doi.org/10.1063/5.0236614>

I. INTRODUCTION

Cuprous halides are a class of ionic semiconductors with diverse potential in electronic and optoelectronic applications.¹ The cuprous atoms are arranged in a face-centered cubic (fcc) lattice, while halogen atoms occupy the four nearest neighboring sites, resulting in the zinc-blende (γ -phase) structure at room temperature. These materials exhibit significantly large exciton binding energies, which contributes to the high quantum efficiencies of the light-emitting devices compared to III-nitrides. This makes them favorable for various optoelectronic applications with high optical gain, including light-emitting diodes (LEDs), photodiodes, touchscreens, and flat panel displays.²

Additionally, cuprous halides exhibit a wide bandgap of approximately 2.9–3.4 eV, with variations depending on experimental measurements.^{3–6} Based on the experimental bandgap value, these materials commonly possess a bulk breakdown field of around 3000 kV/cm (theoretically estimated from Ref. 7). This suggests that cuprous halides hold significant potential as wide bandgap semiconductors (WBSs), positioning them as promising candidates for high-power electronic device applications.

To enable widespread utilization and enhanced performance of cuprous halides, high-quality single-crystalline forms of the

materials have become essential, driving the advancement of various crystal growth techniques to meet these demands. Consequently, diverse crystal growth methods have evolved, yielding improved crystal structures.^{8–13} This evolution is expected to establish a new platform for enhanced optoelectronic and electronic functionalities. In this context, understanding the transport characteristics of cuprous halides is crucial guidance.

However, there remains a lack of thorough theoretical investigation into the high-field transport properties of cuprous halides. Only limited studies using tight-binding models for electron transport exist.¹⁴ In this paper, we present the high-field transport properties of electrons and holes in CuCl, CuBr, and CuI from a first-principles analysis. Ensemble Monte Carlo (EMC) transport simulations¹⁵ based on scattering rates derived from electron-phonon coupling calculations using density functional perturbation theory (DFPT) are adopted to analyze the high-field behaviors of carriers.

II. ELECTRON AND PHONON PROPERTIES OF CUPROUS HALIDES

Electronic band structures and phonon dispersions were calculated using DFT and DFPT. QUANTUM ESPRESSO DFT suite

20 September 2025 15:55:32

was used under generalized gradient approximation (GGA) with the Perdew–Burke–Ernzerhof (PBE) exchange correlation.¹⁶ Methodologically, tight-binding approximations and hybrid functional approaches could also be considered in relation to the accurate prediction of electronic band structure properties such as bandgap. However, incorporating spin-orbit coupling (SOC) in tight-binding models presents challenges that may not capture the full complexity of SOC effects. Although hybrid functional pseudopotentials can improve the treatment of SOC, they complicate the calculation of electron–phonon interactions and are incompatible with DFPT. Therefore, we chose to utilize the suggested approach, which provides a comprehensive framework for accurately calculating the electronic structure, including SOC effects, alongside reliable treatment of electron–phonon interactions.

Optimized norm-conserving Vanderbilt (ONCV) pseudopotentials were adopted for copper and halides.¹⁷ An $8 \times 8 \times 8$ Monkhorst–Pack (MP) grid was used for the Brillouin-zone sampling in electronic and phonon calculations. The plane wave cut-off energy was set to 120 Ry after careful convergence study.¹⁸ For the subsequent electron–phonon coupling calculations, all computations were conducted using these well-converged parameters. Our lattice optimization process includes probing optimum lattice constant and atomic configuration that minimize total system energy and pressure. The analysis of lattice optimization reveals that the zinc-blende structural lattice constants for CuCl, CuBr, and CuI are 5.42, 5.7, and 6.09 Å, respectively, demonstrating good agreement with experimental results.¹⁹

The electronic configuration of Cu is $[\text{Ar}]3d^{10}4s^1$ while that of Cl is $[\text{Ne}]3s^23p^5$. The configurations of Br and I are $[\text{X}](\text{Y}-1)d^{10}\text{Y}s^2\text{Y}p^5$, where X is Ar and Kr, and Y is 4 and 5, respectively. When Cu and one halide form the zinc-blende structure, d -orbital is fully occupied, leaving eight valence electrons in s - and p -orbitals for two atoms in the fcc unit cell, similar to III–V zinc-blende crystals. From $k \cdot p$ theory, it is known that III–V compounds have eight valence electrons forming four spin-degenerate energy bands: conduction, heavy hole (HH), light hole (LH), and split-off (SO). Similarly, Cu-halides show analogous arrangements of the conduction and valence bands to III–V compounds. However, the details differ significantly, particularly in valence bands when spin-orbit coupling (SOC) is considered.

The calculated electronic band structures without SOC for CuCl, CuBr, and CuI are shown in Figs. 1(a)–1(c), respectively. Our calculations indicate that all cuprous halides exhibit direct bandgaps, similar to III–V materials, with values of 0.52, 0.41, and 1.07 eV for CuCl, CuBr, and CuI, respectively. The calculated bandgaps align with previous GGA-based calculations,^{20,21} though these values are smaller than the experimental measurements^{4,22} due to the limitations of density functional theory (DFT).²³ Regarding the carrier transport, two features are distinctively noticeable. All studied materials have a threefold degeneracy at the valence band maximum (VBM): HH, LH, and SO. These evolve to a twofold degenerate state and a single state along the Γ -L and Γ -X directions, while degeneracy vanishes along the Γ -K direction. In the conduction bands, satellite valleys exist, which can influence the transport characteristics.

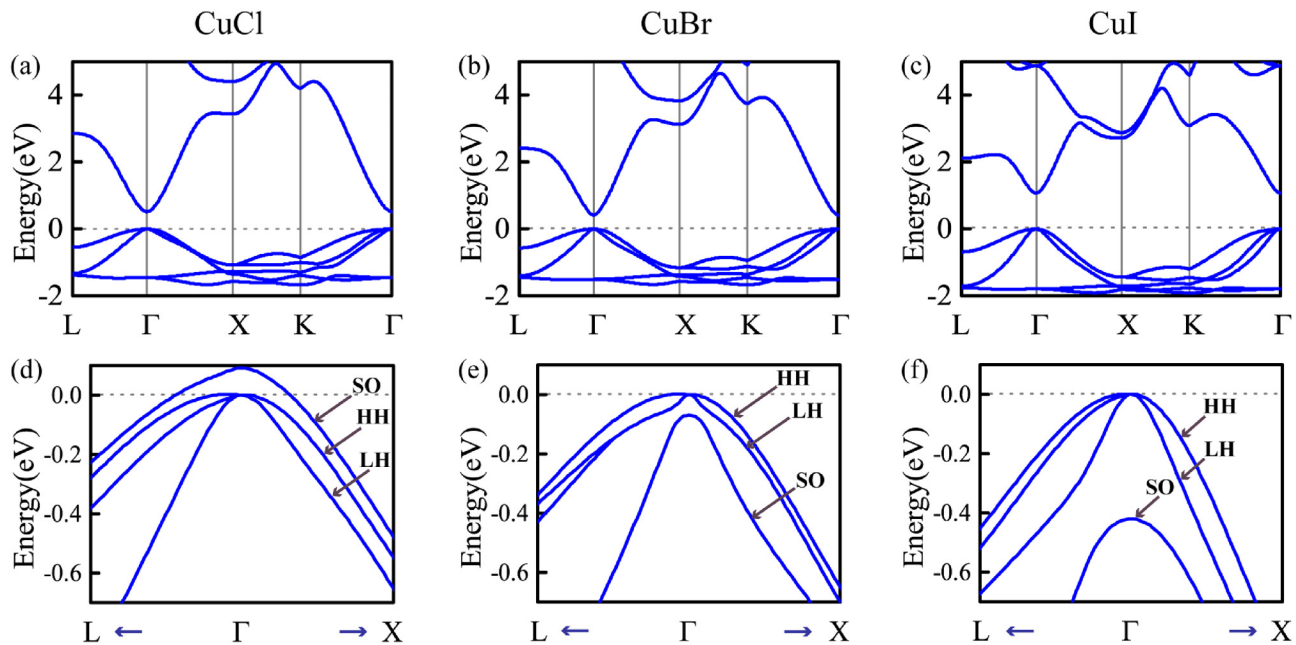


FIG. 1. Electronic band structures of cuprous halides. (a)–(c) represent CuCl, CuBr and CuI, respectively, without SOC. (d)–(f) are valence bands of CuCl, CuBr, and CuI considering SOC near Γ .

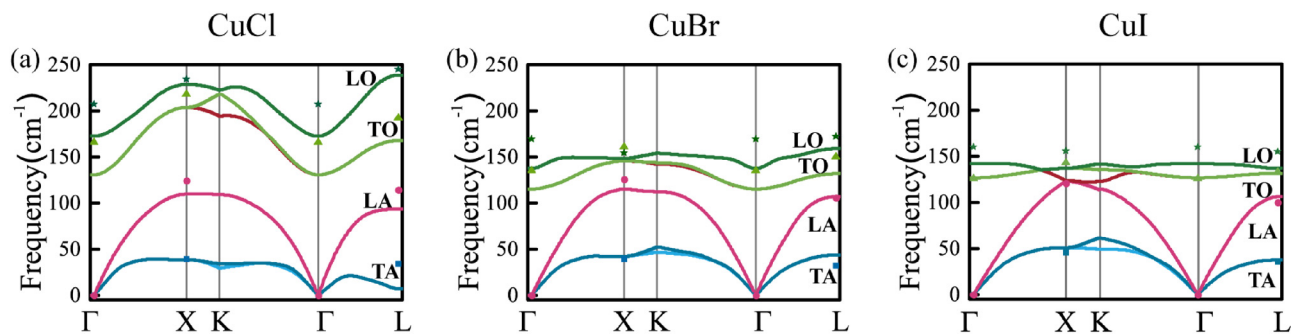


FIG. 2. Phonon dispersions of cuprous halides. (a)–(c) represent CuCl, CuBr, and CuI. Experimental measurements taken from Refs. 26–28 at a high symmetry point are marked with symbols.

Figures 1(d)–1(f) show the valence band structure with the SOC effect. The energy bands around VBM are highlighted since SOC strongly influences the valence band structures, which may substantially affect hole transport. In contrast, the conduction band splitting by SOC has little influence on the band structure. For this calculation, fully relativistic ONCV pseudopotentials were adopted from PseudoDojo.²⁴ The effects of SOC are most pronounced in CuI. The splitting between HH and SO bands in CuI is 0.42 eV, the highest among the investigated materials. The separation between HH and LH in CuI is negligible at Γ , but the curvatures, connected to the effective mass, show clear distinctions. Of particular interest is the band inversion in CuCl. The SO band of CuCl is 0.08 eV higher than the HH and LH bands at Γ , aligning well with the previous experimental observations.^{22,25} On the other hand, CuBr shows a similar trend in the band structure to CuI, without a band inversion, but the SO band separation is relatively small, with only 0.07 eV separation at Γ . The HH, LH, and SO bands are generally doubly degenerate, yet along Γ -L, HH bands of CuCl and CuI show splitting between spins, appearing as four bands. In the transport calculation, these bands are treated using a *modified three-band model*, where the spin-split bands were averaged. This part will be explained in further detail in the transport section.

TABLE I. Phonon frequencies (cm^{-1}) at a high symmetry point of the FBZ. Experimental data shown in parentheses taken from references. For CuCl, experimental values from Ref. 26 measured at 4.2 K. Experimental values from Ref. 27 measured at 77 K for CuBr. Experimental values from Ref. 28 of CuI measured at room temperature.

K points		TA	LA	TO	LO
CuCl	Γ	0	0	131 (166)	173 (207)
	X	39 (39)	110 (124)	204 (218)	229 (234)
CuBr	Γ	0	0	116 (135)	138 (169)
	X	42 (39)	115 (126)	147 (161)	149 (154)
CuI	Γ	0	0	127 (126)	142 (160)
	L	38 (36)	106 (100)	132 (133)	137 (155)
	X	51 (46)	123 (121)	124 (143)	137 (156)

Figure 2 presents the phonon dispersions of CuCl, CuBr, and CuI. In the zinc-blende structure of cuprous halides, there are two atoms per unit cell, resulting in six phonon modes: two transverse acoustic (TA) modes, one longitudinal acoustic (LA) mode, two transverse optical (TO) modes, and one longitudinal optical (LO) mode. LO–TO splitting, which occurs in a polar semiconductor material, is evident in all calculated phonon dispersions. Notably, CuCl exhibits higher LO phonon energy compared to the other materials, which may affect the polar optical phonon scattering. The calculated phonon frequencies at high-symmetry points are summarized in Table I. Overall, the acoustic phonon frequencies show good agreement with experimental results, whereas small discrepancies (1% ~ 18%) are observed in the optical modes compared to experiments.^{26–28} The discrepancy in LO frequencies at Γ is particularly pronounced (18% in CuBr), which may attribute to differences between theoretical ground state calculations and experimental measurement environments, which cannot avoid the temperature-induced shifts in phonon frequencies.²⁹ The sound velocities, relative static, high-frequency dielectric constants, and densities are summarized in Table II. The calculated sound velocities show excellent agreement with the measured values.³⁰ In the following calculations, experimental dielectric constants and densities were used,^{30–34} to eliminate the possibility of error propagation.

TABLE II. Elastic and optical properties of longitudinal sound velocity, dielectric constant, and density used in the simulation. Available data references are listed for the properties.

	ν_{LA} (10^3 cm/s)	ϵ_∞	ϵ_0	Density (g/cm^3)
CuCl	356 (363) ^a	3.61 ^a	7.90 ^b	4.14 ^a
CuBr	345 (338) ^a	4.06 ^a	7.90 ^a	4.72 ^a
CuI	307 (303) ^{c,d}	4.50 ^e	6.50 ^d	5.67 ^a

^aReference 30.

^bReference 31.

^cReference 32.

^dReference 33.

^eReference 34.

20 September 2025 15:55:32

III. CARRIER-PHONON INTERACTIONS

The carrier (electron and hole)-phonon scattering rates are essential for transport analysis, as they depend on the interaction strength between carriers and phonons. The Electron-Phonon Wannier (EPW) program was used to estimate the interaction strength, where maximally localized Wannier functions are interpolated to calculate the carrier-phonon coupling matrices.^{35–37} The electron-phonon interaction matrix element can be read as

$$g_{mn}^v(k, q) = \sqrt{\frac{\hbar}{2m_0\omega_{vq}}} \psi_{mk+q} | \delta_{qv} V(r) | \psi_{nq} = \sqrt{\frac{\hbar}{2m_0\omega_{vq}}} M_{mn}^v(k, q), \quad (1)$$

where m_0 is the sum of all atomic masses in a unit cell and ω_{vq} is the frequency corresponding to a phonon vector q . $M_{mn}^v(k, q) = \psi_{mk+q} | \delta_{qv} V(r) | \psi_{nq}$, which can be evaluated using ψ_{nq} and ψ_{mk+q} , the wave functions of the initial and final states with the wave vector k and $k + q$, respectively. Here, n and m denote band indices and $\delta_{qv} V(r)$ represents the perturbation potential.

The carrier-phonon interaction strengths were calculated using the Wannier function and atomic force constant approaches. Initial electronic states were chosen to include the key valleys that need to be considered for both the conduction band bottom and the valence band top, as a function of phonon wave vector. For the conduction band, Γ and the satellite valleys were considered for each material. Conversely, only states at the Γ point with three bands (HH, LH, and SO bands) were considered for the valence band due to the absence of satellite valleys. The electron-phonon coupling matrices were computed for each phonon dispersion across the entire first Brillouin zone (FBZ). Figure 3 displays the calculated electron-phonon and heavy hole-phonon coupling matrix elements as a function of phonon wave vector (q_x, q_y) on the $q_z = 0$ plane. The most significant contributing phonon branches and initial electronic states were selected for plotting. All the matrix elements in Fig. 3 exhibit reflection symmetry along the $q_x = q_y$ axis and show pronounced interactions near Γ . Among the materials, CuCl demonstrates the strongest interaction strength, while CuI shows the weakest. Given that all the studied cuprous halides possess a zinc-blende structure and adhere to cubic symmetry, VBM and conduction band minimum (CBM) near the Γ point

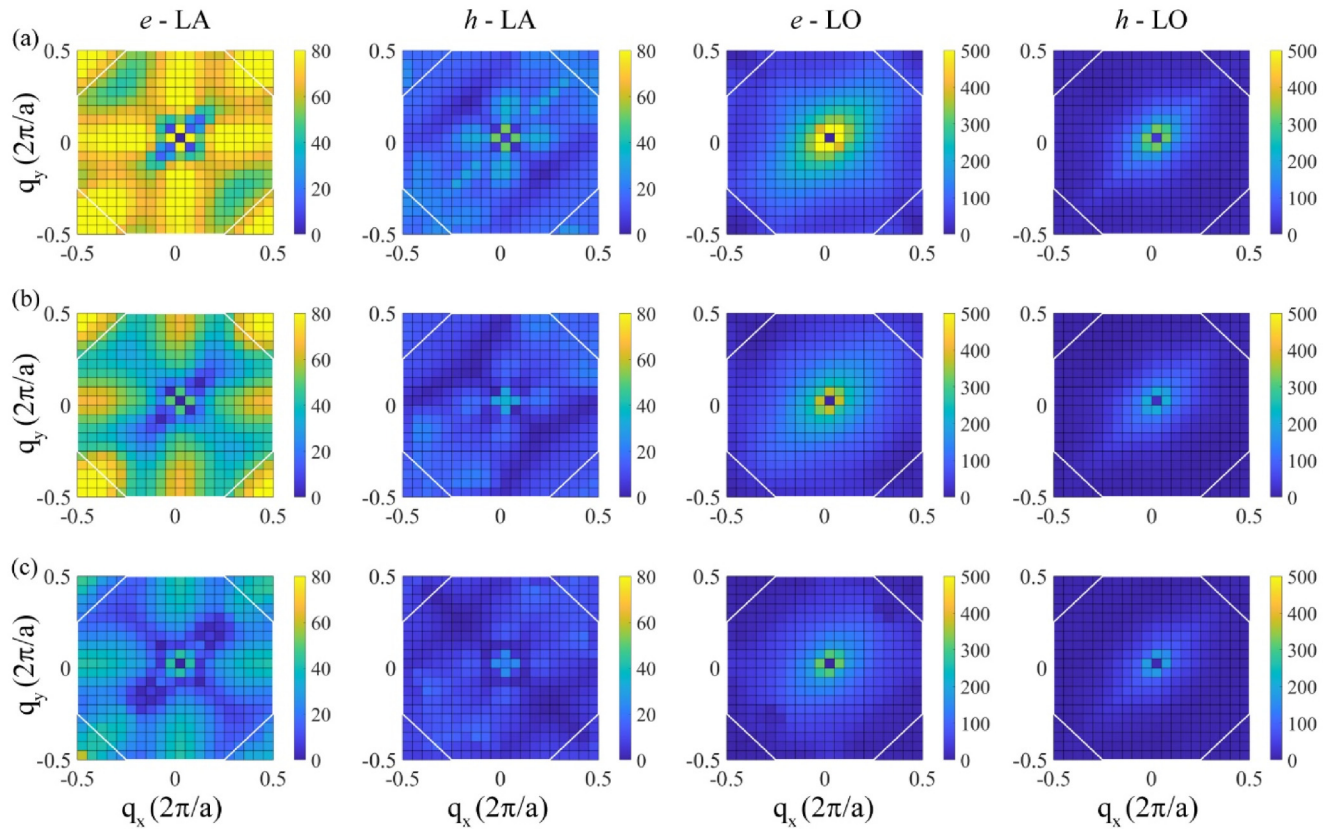


FIG. 3. Carrier-phonon interaction matrix elements in the units of meV as a function of phonon wave vector q for electrons and holes in FBZ at the $q_z = 0$ plane. Only matrix elements with significant results are presented (initial electronic state $k = \Gamma$ with LA and LO phonon modes). (a) for CuCl, (b) for CuBr, and (c) for CuI. White lines in the figures indicate FBZ.

20 September 2025 15:55:32

exhibit weak coupling with transverse phonons.^{38–40} Consequently, longitudinal phonons, which predominantly contribute to the carrier scatterings, were considered in the following transport calculations.

Deformation potentials, which are primarily determined by carrier–phonon coupling matrix elements and the structural elastic properties, can be deduced for each valley and crystallographic direction from these interaction matrices. The acoustic deformation potential (ADP) and the optical deformation potential (ODP) theories are well-established in the literature.^{41,42} In the limit of long-wavelength phonons, the slope of $M_{mn}^v(k, q)$ with respect to $|q|$ corresponds to the first-order ADP. For optical phonons, $M_{mn}^v(k, q)$ represents the zero-order ODP. $M_{mn}^v(k, q)$ were numerically calculated from the computed $g_{mn}^v(k, q)$. Specifically, the ADPs and ODPs can be calculated as

$$D_{ADP} = \frac{1}{|q|} \times g_{mn}^v(k, q) / \sqrt{\frac{\hbar}{2m_0\omega_{vq}}}, \quad (2)$$

$$D_{ODP} = g_{mn}^v(k, q) / \sqrt{\frac{\hbar}{2m_0\omega_{vq}}}. \quad (3)$$

Intravalley scattering involves small q acoustic phonons interacting with carriers at high-symmetry points (valleys). the interaction energies of carriers with TA and LA phonons were summed up to calculate the intravalley deformation potentials. Optical phonons also participate in intravalley scattering. Similarly, the deformation potentials for the intervalley scattering were calculated by summing interaction energies with longitudinal and transverse phonon modes. All possible intervalley transitions between valleys were taken into account for the conduction band, whereas intervalley scatterings in the valence bands were omitted due to the absence of the satellite valleys. Instead, interband scatterings among the three bands (HH, LH, and SO) at Γ were considered. The calculated intra- and intervalley deformation potentials for each material are summarized in Tables III and IV.

Handling the anisotropy of electron–phonon matrix elements is a crucial factor in accurately capturing the angle of scattering processes during transport. In the case of cuprous halides, the Γ valley plays a dominant role in transport, and since the Γ valley is both spherical and isotropic, the angular dependence of the deformation potential is expected to have minimal impact. This implies that anisotropy in the electron–phonon matrix elements will have a negligible effect on electron transport, making our single deformation potential approach, which simplifies the treatment of matrix elements and deformation potentials, sufficient to predict the essential transport characteristics.

IV. ENSEMBLE MONTE CARLO CARRIER TRANSPORT

The carrier transport properties were analyzed using the EMC transport simulation. Based on Fermi's golden rule, the total

TABLE III. Estimated deformation potential constants of electron–phonon interaction in the conduction band bottom at a high symmetry point of the FBZ. Symbols “ac” and “op” refer the acoustic and optical phonons, respectively.

Electron transition	Phonon mode	CuCl	CuBr	CuI	Units
$\Gamma \rightarrow \Gamma$	ac	4.4	2.9	2.9	eV
	op	0.021	0.017	0.018	eV
$\Gamma \rightarrow L$	ac	0.55	10^{10} eV/m
	op	0.042	eV
$\Gamma \rightarrow X$	ac	0.088	0.086	0.059	eV
	op	0	0	0	10^{10} eV/m
$L \rightarrow L$	ac	3.2	eV
	op	0.017	eV
$L \rightarrow L'$	ac	0.050	eV
	op	0.67	10^{10} eV/m
$L \rightarrow X$	ac	0.016	eV
	op	1.2	10^{10} eV/m
$X \rightarrow X$	ac	3.9	3.0	2.3	eV
	op	0.028	0.018	0.017	eV
$X \rightarrow X'$	ac	0.17	0.15	0.12	eV
	op	0	0	0	10^{10} eV/m

scattering rate is calculated as

$$\Gamma(k) = \frac{2\pi}{\hbar} \sum_{k'} |M(k, k')|^2 \delta(E_k - E_{k'} \pm \hbar\omega_q), \quad (4)$$

where $M(k, k')$ represents the matrix element between initial (k) and final (k') states. E_k and $E_{k'}$ are the corresponding energies, and $\hbar\omega_q$ denotes the phonon energy. The delta function $\delta(E_k - E_{k'} \pm \hbar\omega_q)$ enforces the selection rule by the energy conservation in the scattering event. The scattering mechanisms incorporated in the EMC simulations include phonon and ionized impurity scatterings. Phonon scattering mechanisms encompass acoustic phonon (AP) and polar

TABLE IV. Estimated deformation potentials of hole–phonon interaction in the valence band at a high symmetry point of the FBZ.

Hole transition	Phonon mode	CuCl	CuBr	CuI	Units
HH \rightarrow HH	ac	3.0	2.0	1.8	eV
	op	0.021	0.017	0.018	eV
HH \rightarrow LH	ac	0.053	0.032	0.023	eV
	op	5.0	3.1	3.3	10^{10} eV/m
HH \rightarrow SO	ac	0.053	0.032	0.023	eV
	op	5.0	3.1	3.3	10^{10} eV/m
LH \rightarrow LH	ac	2.9	2.0	1.8	eV
	op	0.021	0.017	0.018	eV
LH \rightarrow SO	ac	0.055	0.031	0.023	eV
	op	5.0	3.1	3.3	10^{10} eV/m
SO \rightarrow SO	Ac	2.5	1.9	1.7	eV
	Op	0.021	0.017	0.018	eV

20 September 2025 15:55:32

optical phonon (POP) scattering. For the ionized impurity (II) scattering, the Brooks–Herring model with the screening potential is employed to model the Coulomb scattering process involving ionized donors and acceptor impurities.⁴³ As outlined in Sec. III, the conduction and valence bands of cuprous halides display contrasting features, such as satellite valleys in the conduction band and degeneracy lift-up due to SOC in the valence bands. These differences necessitate two distinct approaches in EMC simulations. An electric field was applied along the [001] direction, and since the energy bands are relatively isotropic near Γ , minimal dependence on the field direction is anticipated.

The conduction band was described using a *three-valley model* with non-parabolicity for CuI, while a *two-valley model* was applied for CuCl and CuBr. An intriguing finding of our study is the distinct conduction band structures among the cuprous halides. In CuI, local energy minima, or valleys, are observed at both the L and X points, where relatively larger electron population can exist. However, in CuCl and CuBr, no L valley was identified. Our calculations indicate that the effective mass near the L point in CuCl and CuBr turns out to be negative along the [111] direction but positive along the [001] and [011] directions. This suggests that the energy bands near L in CuCl and CuBr act as saddle points, rather than valleys, as previously investigated.⁴⁴ Consequently, only two valleys (Γ and X) were considered in the transport calculations for CuCl and CuBr. In CuI, the L and X valley are located 1.041 and 1.65 eV above from the Γ valley, respectively. In CuCl and CuBr, the valley separations between X and Γ are 2.919 and 2.72 eV, respectively.

The non-parabolicity of the conduction band was accounted for using Eq. (4), which is expressed as

$$E(k)\{1 + \alpha E(k)\} = \frac{\hbar^2 k^2}{2m^*}, \quad (5)$$

where α is the non-parabolicity factor and m^* is the effective mass at Γ . This model, driven from the $k \cdot p$ method, is known to improve the accuracy of the E - k relation in high-field transport as well as the computational efficiency.⁴⁵ The factor α was obtained

using the Kane model,⁴⁶

$$\alpha = \frac{1}{E_g} \left(1 - \frac{m^*}{m_0} \right)^2, \quad (6)$$

where E_g is the energy gap and m_0 is the electron rest mass. The effective masses of each valley were calculated using the definition ($m^* = [\partial^2 E(k)/\hbar^2 k^2]^{-1}$). For the elliptic satellite valleys at X and L, the harmonic mean of the effective masses along the principal axis was used, which is given by

$$m^* = 3 \left(\frac{1}{m_l^*} + \frac{1}{m_{t1}^*} + \frac{1}{m_{t2}^*} \right)^{-1}, \quad (7)$$

where m_l^* is the longitudinal effective mass and m_t^* is the transverse effective mass. The obtained non-parabolicity factors and effective masses for each valley are summarized in Table V.^{21,47–49}

The valence bands were described using a *modified three-band* model to account for HH, LH, and SO bands. In the case of HH bands, which exhibit spin splitting along the Γ -L direction, averaging technique was applied as previously discussed. Since Eq. (4) poorly captures the non-parabolicity of HH and LH bands, these bands require special treatment due to their non-parabolic and warped shapes.^{50,51} On the other hand, the SO band can be adequately described using a parabolic band model with an estimated effective mass. The effective masses of SO bands were calculated to be 0.64, 0.23, and 0.6 in units of m_0 for CuCl, CuBr, and CuI, respectively.

For HH and LH bands, the analytical expressions derived for the zinc-blende crystal by the $k \cdot p$ method framework can address the non-parabolicity and warping of the valence band dispersion.^{50–53} The energy dispersion can be described by the following expression:

$$E(k) = \frac{\hbar^2 k^2}{2m_0} |A| (1 \mp g(\theta, \phi)) \chi(E) \\ = \frac{\hbar^2}{2m_0} \left(Ak^2 \mp (B^2 k^4 + C^2 (k_x^2 k_y^2 + k_y^2 k_z^2 + k_z^2 k_x^2))^{\frac{1}{2}} \right) \chi(E). \quad (8)$$

TABLE V. Structural properties of effective masses (unit of m_0) and non-parabolicity factors. Available experimental measurements and *ab initio* calculation references are presented.

	K points	m_{001}^*	m_{011}^*	m_{111}^*	m^* (Reference)	α (eV ⁻¹)
CuCl	Γ	0.30	0.32	0.31	0.50 ^a , 0.43 ^b	0.14
	X	5.1	0.54	0.70		
CuBr	Γ	0.22	0.24	0.21	0.28 ^{a,b}	0.20
	X	1.9	0.49	0.59		
CuI	Γ	0.20 (0.19 ^c)	0.20 (0.20 ^c)	0.19 (0.20 ^c)	0.26 ^d , 0.3 ^a , 0.33 ^b	0.21
	L	0.35	0.62	3.6		
	X	1.8	0.43	0.74		

^aReference 47 (experiment).

^bReference 48 (experiment).

^cReference 21 (GGA).

^dReference 49 (tight binding approximation).

20 September 2025 15:55:32

Here, the upper and lower signs represent HH and LH bands, respectively. This will be case in the following, too. The function χ , known as the non-parabolicity function, is given by

$$\chi(E) = \frac{aE^2 + bE + c}{dE + 1}, \quad (9)$$

where a , b , c , and d are certain parameters to fit the analytical function to each band over the intended energy range. The final expression for the energy dispersion can be found as

$$E = \frac{(-bfk^2 + 1) - \sqrt{((bfk^2 - 1)^2 - 4(afk^2 - d)cfk^2)}}{2(afk^2 - d)}. \quad (10)$$

Here, f is the angular part of the dispersion relation, which reads as

$$f = \frac{\hbar^2}{2m_0} |A|(1 \mp g(\theta, \phi)), \quad (11)$$

and $g(\theta, \phi)$ is given as

$$g(\theta, \phi) = \left(\left(\frac{B}{A} \right)^2 + \left(\frac{C}{A} \right)^2 (\sin^4 \theta \cos^2 \phi \sin^2 \phi + \sin^2 \theta \cos^2 \theta) \right)^{\frac{1}{2}}, \quad (12)$$

where A , B , and C are Dresselhaus parameters.

The Dresselhaus parameters were determined by fitting Eq. (8) to the DFT-calculated HH and LH bands near the Γ point. The fitting process aimed to find the optimal set of parameters that accurately describe both bands. Using the extracted values of A , B , and C , the parameters a , b , c and d for the non-parabolic energy dispersion function [Eq. (12)] were subsequently obtained. These extracted parameters are summarized in Tables VI and VII, respectively. Each band is characterized by its own unique non-parabolic function. To mitigate directional dependencies, averaged values of both energy and non-parabolicity were employed at each point. By dividing the energy range into small intervals, we identified sets of parameters that best fit the non-parabolic function. A detailed explanation of this methodology is available in previous research.⁵⁴ In the case of CuCl, due to the presence of an inverted split-off band and threefold bands, distinct parameter sets were extracted and are presented in Table VI.

During the EMC simulation process, after initializing the carrier energy and momentum, scattering rate tables were

TABLE VI. Extracted Dresselhaus parameter used in the simulation.

	A	B	C
CuCl	1.18	0.42	1.63
	1.27	0.62	1.34
CuBr	2.65	1.75	2.69
CuI	2.93	1.30	3.22

TABLE VII. Non-parabolic function parameters a , b , c , and d , which comprise an analytical expression describing the non-parabolicity as a function of energy.

		Energy range (eV)	a (eV ⁻²)	b (eV ⁻¹)	c	d (eV ⁻¹)
CuCl	HH	0.000–0.100	4.49	24.0	2.26	44.3
		0.100–0.550	−73.9	115	3.77	159
		0.550–0.750	0.617	−1.48	0.792	−1.23
		0.750–1.00	1.64	−3.02	1.37	−1.24
	HH'	0.000–0.040	0.099	0.998	0.892	0.003
		0.040–0.100	−3.84	1.57	0.927	1.56
		0.100–0.600	−5.91	8.52	0.952	9.26
CuBr	HH	0.600–1.00	0.747	−1.81	0.990	−1.19
		0.000–0.040	−118	6.63	0.659	−4.12
		0.040–0.110	−20.2	21.9	0.740	19.9
		0.110–0.600	−1.24	1.28	0.947	1.55
		0.600–0.800	0.712	−1.85	1.08	−1.10
	LH	0.800–1.00	2.00	−3.89	1.86	−1.16
		0.000–0.110	186	−37.6	2.26	3.22
		0.110–0.310	12.9	9.25	2.96	145
		0.310–0.700	−13.3	20.1	0.416	110
		0.700–1.00	0.123	−0.316	0.190	−1.03
CuI	HH	0.000–0.040	7.81	254	0.299	286
		0.040–0.100	−91.5	169	0.311	180
		0.100–0.750	−1.11	1.59	0.889	2.02
		0.750–1.00	0.380	−1.25	0.943	−0.820
	LH	0.000–0.100	5.33	−3.32	1.09	−1.08
		0.100–0.500	2.14	−2.85	1.10	−0.821
		0.500–0.900	−1.63	−1.43	18.8	96.9
		0.900–1.00	0.204	−0.582	0.406	−0.820

generated. These tables stored the calculated scattering rates, indexed by valleys, bands, scattering mechanisms, and carrier energies. After a scattering-free acceleration by the external electric field for a very short time (\sim fs), scattering mechanisms were randomly selected from the scattering tables as a scattering event occurred. Utilizing the previously calculated parameters, we employed the proposed EMC transport simulation to investigate carrier transport in cuprous halides. The total transport time was set to 10 ps, and the current was estimated every femtosecond by averaging over an ensemble of 20 000 particles. The influences of the electric field and temperature variations were studied with a doping concentration of 10^{17} cm^{-3} for both electrons and holes. Further details about the EMC transport methods are thoroughly documented in Refs. 55–61.

Clearly, there is a distinction in accuracy between full band MC calculations, which account for the anisotropy of electron-phonon matrix elements and deformation potentials, and our analytical MC modeling approach. However, within the scope of this study, the gap between the two methods is not anticipated to be significant. There are also prior studies that have successfully employed analytical modeling to predict carrier transport characteristics in semiconductor materials.^{51–55} Furthermore, experimental measurements of transport properties also contain inherent uncertainties, and our analytical predictions are expected to fall

within the experimental ranges. Thus, this computationally efficient and effective method was employed to strike a balance between precision and feasibility.

V. RESULTS AND DISCUSSION

First, the transient response of the carrier was examined, and the time evolution of electron velocity in CuI under different electric fields is presented in Fig. 4 as an example. Overshoot in ballistic velocity is typically observed only when the applied field surpasses the steady-state field at which the peak in electron drift velocity occurs.⁶² In Fig. 4(a), it is evident that the velocity overshoot initiates between 30 and 40 kV/cm. This range aligns with the v_d peak shown in Fig. 5(c). An intriguing observation in Fig. 4(b) is that the velocity overshoot at high electric fields is quite substantial, and the saturation of the velocity requires a relatively longer time. Conversely, at low electric fields, dominant POP scattering makes the drift velocity uniform, allowing the steady state to

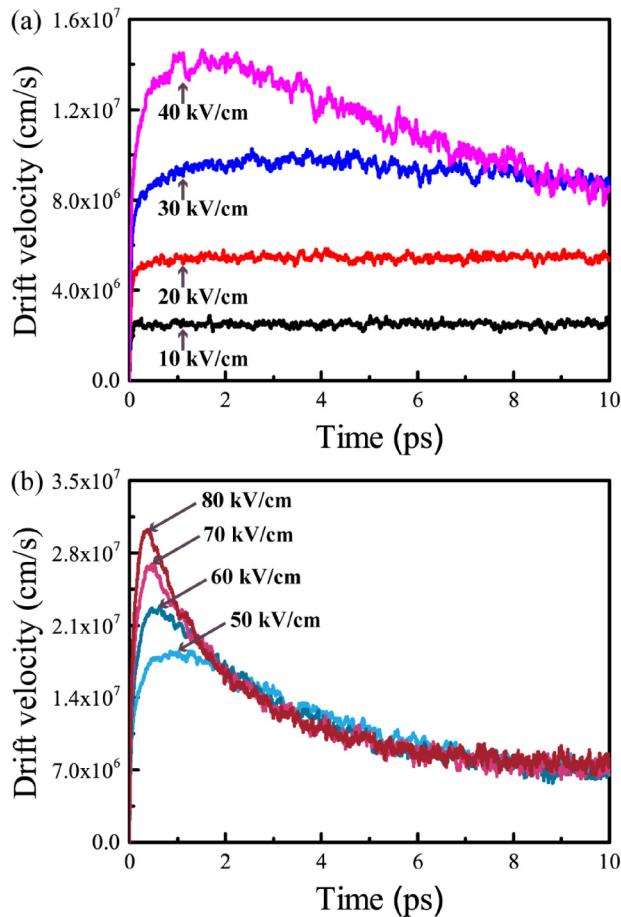


FIG. 4. Time evolution of the electron velocity in CuI for different electric fields applied. The applied electric field was increased by 10 kV/cm from 10 to 40 kV/cm in (a) and 50 to 80 kV/cm in (b). $T = 300$ K with $N_d = 10^{17} \text{ cm}^{-3}$.

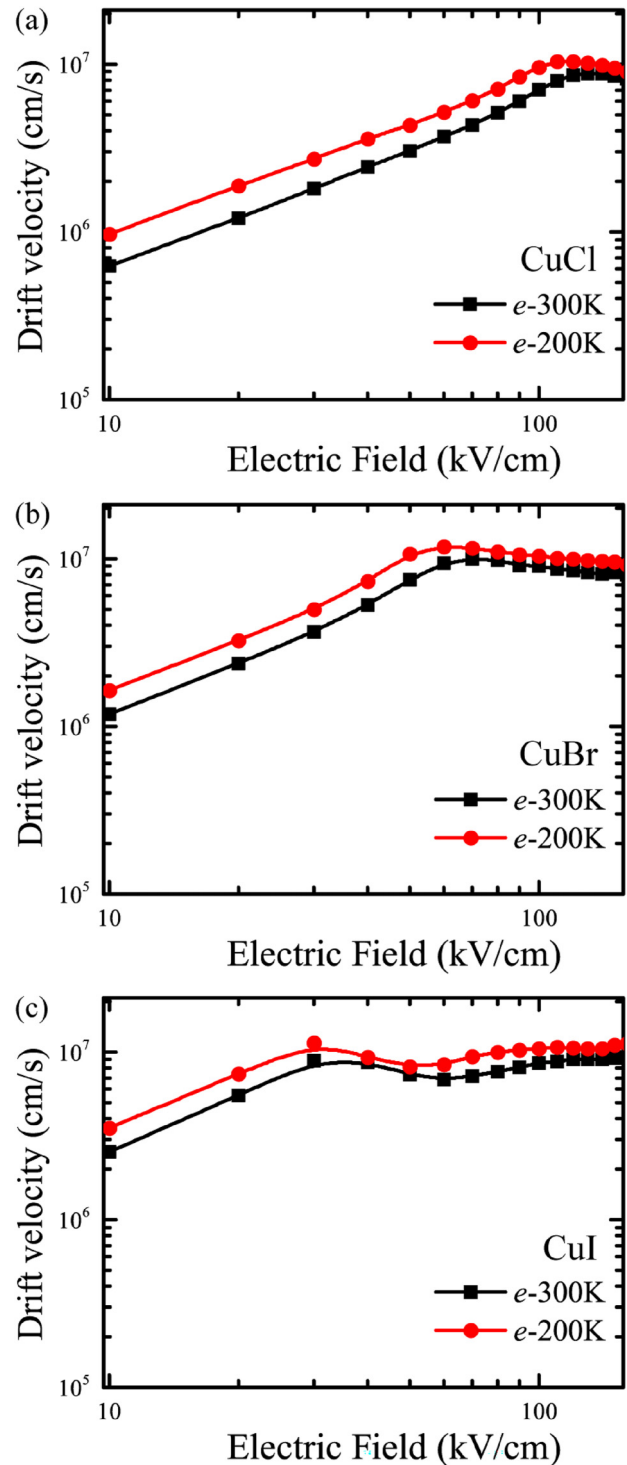


FIG. 5. Electron drift velocity vs electric field characteristics in (a) CuCl, (b) CuBr, (c) CuI at different temperatures in a logarithmic coordinate. $N_d = 10^{17} \text{ cm}^{-3}$.

20 September 2025 15:55:32

be achieved quickly. However, beyond 40 kV/cm, the velocity overshoot becomes pronounced. This may be caused by the significant contribution from intraband scattering with increased carrier energy, which aligns with the previous transport study on β -Ga₂O₃.⁶³ The facilitated short-range transitions by intraband scattering substantially enhance momentum relaxation, while energy relaxation remains limited due to the small phonon energy involved in intraband scattering. This disparity between the two relaxation rates results in a slow increase in carrier energy compared to the drift velocity. The momentum relaxation rate also depends on carrier energy and requires a longer time to adjust than momentum, leading to a large transient velocity overshoot.⁵⁷ After a period in which energy relaxation becomes effective in spreading the energy distribution, the drift velocity starts decreasing and finally reaches the steady state.

Figure 5 illustrates the drift velocity (v_d) of electrons as a function of the applied electric field at different temperatures. During the carrier mobility calculations, an electric field of 10 kV/cm was applied, and the drift velocity was averaged over the simulation window from 9 to 10 ps. It is worth to note the presence of inherent statistical errors in MC simulation results. For instance, under the above applied field, the averaged drift velocities over the 1 ps window were 6.25×10^5 , 1.18×10^6 , and 2.54×10^6 cm/s, with corresponding standard deviations of 8.32×10^4 , 9.17×10^4 , and 1.03×10^5 cm/s, respectively. The resulting calculated electron mobilities (μ_e) were 62.5, 118, and 254 cm²/V s at 300 K for CuCl, CuBr, and CuI, respectively. The v_d peaks occur at 130, 70, and 35 kV/cm for CuCl, CuBr, and CuI, respectively. The saturation velocity (v_{sat}) was 8.20×10^6 and 9.10×10^6 cm/s for CuBr and CuI, respectively. Interestingly, within the examined electric field range of 10–150 kV/cm in CuCl, no velocity saturation was observed; instead, only a reduction in velocity after the peak was detected. In CuCl, the transfer of electron to the satellite X valley is unlikely due to the substantial energy separation between the X valley and the CBM. Therefore, a v_d reduction by intervalley transition, commonly probed in III–V semiconductors, is not expected. Additionally, in CuCl, substantial intravalley scattering combined with high optical phonon energy results in lower mobility and causes the v_d peak to occur at higher electric fields compared to other materials. As a result, v_d does not reach saturation even at significantly high fields.

Another notable effect is the difference in v_d saturation characteristics between CuBr and CuI. In both materials, the v_d saturations after the peak suggest the presence of negative differential conductivity (NDC), which can be utilized for certain device applications, such as Gunn diode in III–V semiconductors. However, the underlying mechanisms differ from those in materials such as GaAs, where NDC is primarily caused by intervalley scattering. Our investigation reveals that, in CuBr, the velocity saturation and potential NDC arise from short-range intravalley scattering. The large energy separation between sub-valleys in the conduction band ensures that only the Γ valley is involved in electron transport, with minimal contribution from intervalley scattering. Distinct from CuBr, in CuI, the v_d reduction is initiated by carrier transitions to the L valley, which has a lower effective mass. Thus, in CuI, both intervalley scattering and short-range intravalley scattering contribute to the v_d reduction. Notably, due to the energy separation

between Γ and L valleys, this contribution is limited, and a slight increase in v_d after the initial reduction was observed as the field intensity increased. As the field intensifies, the transition of carriers to the L valley becomes more frequent, leading to a gradual increase in v_d . However, beyond a certain field strength, this increase in transitions ceases, resulting in the observed saturation of v_d .

At 200 K, μ_e and v_{sat} increased, whereas the electric fields at which the v_d peak occurs decreased, except for CuCl which does not show the velocity saturation. However, the general trend of the e-field vs v_d relationship remained consistent. More specifically, μ_e improved by 56%, 39%, and 38% for CuCl, CuBr, and CuI, respectively. The largest enhancement in μ_e can be attributed to the significant intravalley small q phonon scattering, which has the highest temperature dependence. Moreover, v_{sat} also increased by 17% and 15% for CuBr and CuI, respectively, while the electric fields around v_d peaks decreased by 15%, 14%, and 14% for CuCl, CuBr, and CuI, respectively. This temperature-dependent trend in transport properties arises from the specific temperature regimes to which the materials' electrons belong. Within the given temperature range, phonon scattering likely dominates over ionized impurity scattering, leading to increased mobility as the temperature decreases.

For hole transport, our analysis reveals that all considered bands (HH, LH, and SO) contribute to the transport. As shown in Fig. 6, the estimated hole-mobilities (μ_h) at 300 K for CuCl, CuBr, and CuI were 14.2, 36.5, and 193 cm²/V s. The associated drift velocities were 1.42×10^5 , 3.65×10^5 , and 1.93×10^6 cm/s at 10 kV/cm, with corresponding standard deviations of 3.11×10^4 , 4.98×10^4 , and 6.89×10^4 cm/s, respectively. In CuBr, a decrease in the slope of the v - F curve with increasing electric field was observed, but no velocity saturation appeared. Velocity saturation was only observed in CuI, where v_d peaks at 50 kV/cm and v_{sat} is around 6.00×10^6 cm/s. This characteristic of hole transport in CuI is due to the larger energy separation of the SO band, which has a heavier effective mass. As the field increases, transitions from HH or LH bands to the SO band occur via interband scattering, leading to a reduction in v_d similar to intervalley transitions in conduction bands. In addition, CuI exhibited a substantially higher μ_h , which stems from the lighter effective masses of the HH and LH bands, along with the large separation of SO. The estimated μ_h for CuI turned out to be exceedingly higher than the experimental value (43.9 cm²/V s at room temperature with hole doping 5×10^{16} cm⁻³),⁶⁴ suggesting potential for improvement as crystal growth techniques advance.

At 200 K, μ_h changed to 4.14, 85.4, and 320 cm²/Vs for CuCl, CuBr, and CuI, respectively. Interestingly, μ_h for CuCl was rather reduced by 70%, while CuBr and CuI displayed the expected behavior, with enhancements of 134% and 67%, respectively. It is well known that at low temperatures, ionized impurity scattering is dominant, and mobility increases as temperature rises since the carrier energy increases, reducing scattering rates. In contrast, at higher temperatures, phonon scattering becomes dominant, leading to decreased carrier mobility as the temperature increases due to the higher phonon population, which increases scattering rates. As shown in Fig. 2, acoustic phonon dispersion of CuCl is similar to that of CuBr and CuI, yet CuCl shows a peculiar temperature

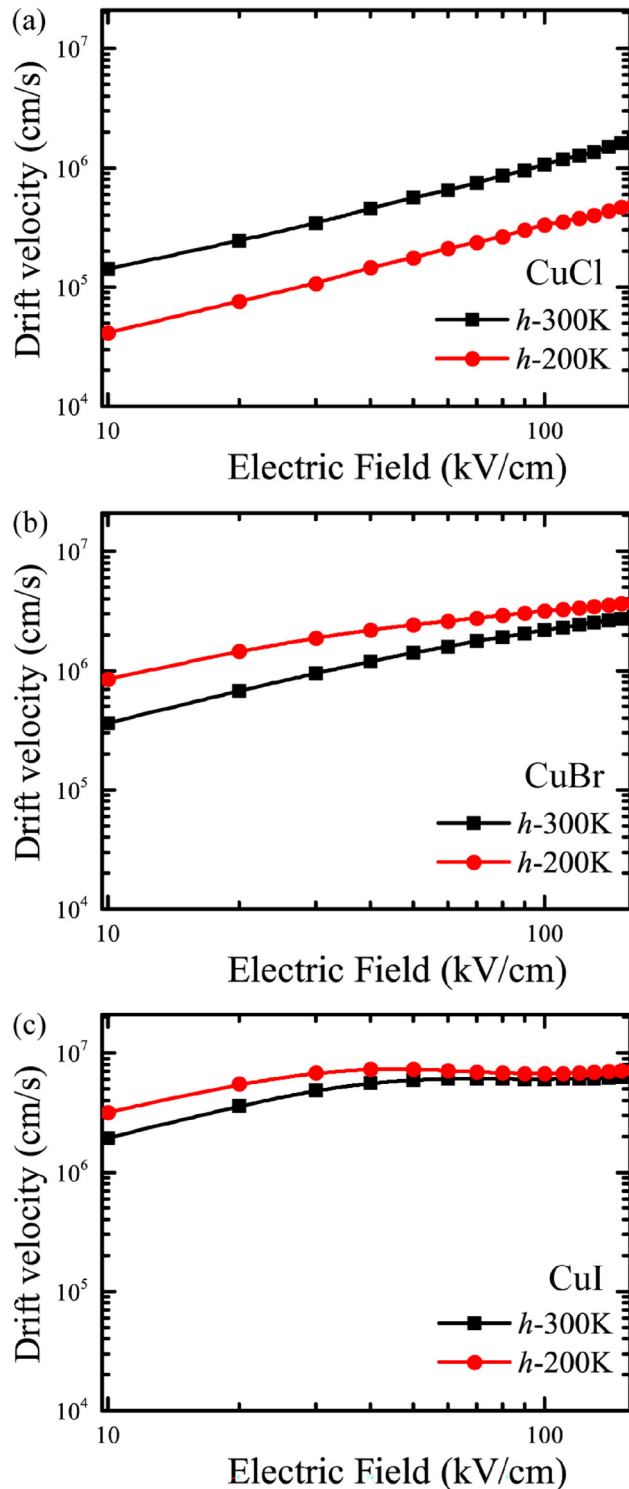


FIG. 6. Hole drift velocity vs electric field characteristics in (a) CuCl, (b) CuBr, (c) CuI at different temperatures. $N_d = 10^{17} \text{ cm}^{-3}$.

TABLE VIII. Transport properties of cuprous halides at 300 K.

		μ (cm^2/Vs)	v_{sat} (10^6 cm/s)	v_d peaks (kV/cm)
CuCl	Electron	62.5	...	130
	Hole	14.2
CuBr	Electron	118	8.20	70.0
	Hole	36.5
CuI	Electron	254	9.10	35.0
	Hole	193	6.00	50.0

dependence only in hole mobility. This unusual temperature dependence in CuCl is primarily attributed to carrier transitions to the third band (LH). The following analysis confirms that as the temperature rises, the carrier population in the LH band increases at a given electric field. Since the LH has the lightest effective mass among the three bands, a larger LH population leads to a higher v_d . Additional simulations for CuCl indicate that μ_h rises with temperature up to 450 K and then starts to decrease as the carrier population in LH saturates and phonon population increases. Other features remain similar to those observed at 300 K: CuBr continues to exhibit a decrease in the characteristic curve, while CuI demonstrates velocity saturation, with v_d peaking at 40 kV/cm and v_{sat} of $7.00 \times 10^6 \text{ cm/s}$.

Table VIII summarizes the transport properties of cuprous halides at 300 K for comparison. In terms of electron transport, CuI exhibits the v_d peak at the lowest electric field, yet it also achieves both the highest v_{sat} and peak velocity. On the other hand, CuCl shows v_d peak at the highest electric field, but it does not display velocity saturation within the given electric field range. These behaviors quite differ from the research of Sekkal and Zaoui,¹⁴ which provided transport characteristics based on the empirical tight-binding method. The differences in these features primarily stem from the electron-phonon interactions and deformation potentials employed in each framework. Our distinct calculations, which include specific electron-phonon scattering mechanisms and intricate energy band structures, may have critically influenced the transport behavior and led to these disparities. Regarding the hole transport, v_{sat} and v_d peak were not observed within the given electric field for both CuCl and CuBr, unlike CuI.

Moreover, CuI stands out with the highest mobilities for both electrons and holes compared to CuCl and CuBr. This is mainly attributed to its relatively smaller effective masses and weaker electron-phonon scattering strengths. The notably high hole-mobility in CuI narrows the gap between electron and hole mobilities (193 vs 254 cm^2/Vs). Different from many semiconductors, which often present significant differences in mobilities—sometimes by orders of magnitude—the similar mobilities for electrons and holes in CuI could be advantageous in applications that require efficient transport of both carrier types. In addition, CuI has been reported as a transparent conducting material (TCM) and successfully utilized as a p-type semiconductor.^{65–68} Combined with its direct wide bandgap based on experimental evidences,⁵ CuI emerges as a promising material for optoelectronic applications with p-type wide bandgap where the response times of both carriers become crucial.

20 September 2025 15:55:32

VI. CONCLUSIONS

We investigated the high-field transport properties of single-crystalline zinc-blende cuprous halides. Despite their similar structures and compositions, these materials exhibit diverse transport characteristics due to subtle differences in their electronic and phononic structures. The valence orbitals of the halides influence the formation of satellite valleys in the conduction bands and the ordering of the HH, LH, and SO bands in the valence bands, leading to marked variations in carrier transport. Our theoretical estimation of high hole mobility in CuI indicates substantial potential for improvement in crystal growth, which could, in turn, pave the way for the development of high-performance p-type wide bandgap optoelectronic devices. Additionally, the unique temperature dependence observed in CuCl, where carrier mobility increases up to 450 K, could be beneficial for high-temperature applications. With reports of large-scale crystalline growth for CuBr and CuI, the cuprous halide family represents a new class of materials with zinc-blende structures similar to III–V compounds, yet with much still to be explored. By providing a deeper understanding of energy transfer mechanisms based on carrier and phonon interactions, our work offers valuable insights for future research directions in this promising class of materials.

ACKNOWLEDGMENTS

This work was supported in parts by Samsung Research Funding and Incubation Center of Samsung Electronics (No. SFRC-IT2102-01) and the National Research Foundation (NRF) grant funded by the Korea government (Ministry of Science and ICT) (Nos. NRF-2021M3F3A2A03017770 and 2022-0-00720-002).

AUTHOR DECLARATIONS

Conflict of Interest

The authors have no conflicts to disclose.

Author Contributions

Min Hyeok Kim: Conceptualization (equal); Data curation (lead); Formal analysis (lead); Investigation (lead); Methodology (equal); Software (lead); Validation (lead); Visualization (lead); Writing – original draft (lead). **Byoung Don Kong:** Conceptualization (lead); Formal analysis (supporting); Funding acquisition (lead); Investigation (supporting); Methodology (equal); Project administration (lead); Resources (lead); Supervision (lead); Validation (supporting); Writing – review & editing (lead).

DATA AVAILABILITY

The data that support the findings of this study are available from the corresponding author upon reasonable request.

REFERENCES

- ¹Á. Balog, G. F. Samu, P. V. Kamat, and C. Janáky, *J. Phys. Chem. Lett.* **10**, 259 (2019).
- ²D. Ahn and S.-H. Park, *Sci. Rep.* **6**, 20718 (2016).
- ³B. Bouhafs, H. Heireche, W. Sekkal, H. Aourag, and M. Certier, *Phys. Lett. A* **240**, 257 (1998).
- ⁴K. Saito, M. Hasuo, T. Hatano, and N. Nagasawa, *Solid State Commun.* **94**, 33 (1995).
- ⁵S. Ves, D. Glötzel, M. Cardona, and H. Overhof, *Phys. Rev. B* **24**, 3073 (1981).
- ⁶J. B. Anthony, A. D. Brothers, and D. W. Lynch, *Phys. Rev. B* **5**, 3189 (1972).
- ⁷W. A. Hadi, M. S. Shur, and S. K. O'Leary, *Solid State Commun.* **356**, 114948 (2022).
- ⁸H. Zhou, X. Chen, T. Zhao, C. Chen, J. Han, S. Pan, and J. Pan, *CrystEngComm* **25**, 1669 (2023).
- ⁹M. Gu, P. Gao, X. L. Liu, S. M. Huang, B. Liu, C. Ni, R. K. Xu, and J. M. Ning, *Mater. Res. Bull.* **45**, 636 (2010).
- ¹⁰Y. Lv, Z. Xu, L. Ye, Z. Zhang, G. Su, and X. Zhuang, *CrystEngComm* **17**, 862 (2015).
- ¹¹S. Koyasu, N. Umezawa, J. D. Baniecki, A. Yamaguchi, and M. Miyauchi, *Cryst. Growth Des.* **18**, 6748 (2018).
- ¹²M. Soga, R. Imaizumi, Y. Kondo, and T. Okabe, *J. Electrochem. Soc.* **114**, 388 (1967).
- ¹³T. Inoue, M. Kuriyama, and H. Komatsu, *J. Cryst. Growth* **112**, 531 (1991).
- ¹⁴W. Sekkal and A. Zaoui, *Phys. B* **315**, 201 (2002).
- ¹⁵C. Jacoboni, *The Monte Carlo Method for Semiconductor Device Simulation* (Springer-Verlag, Vienna, 1989).
- ¹⁶P. Giannozzi, S. Baroni, N. Bonini, M. Calandra, R. Car, C. Cavazzoni, D. Ceresoli, G. L. Chiarotti, M. Cococcioni, I. Dabo, A. Dal Corso, S. de Gironcoli, S. Fabris, G. Fratesi, R. Gebauer, U. Gerstmann, C. Gougoussis, A. Kokalj, M. Lazzeri, L. Martin-Samos, N. Marzari, F. Mauri, R. Mazzarello, S. Paolini, A. Pasquarello, L. Paulatto, C. Sbraccia, S. Scandolo, G. Sclauzero, A. P. Seitsonen, A. Smogunov, P. Umari, and R. M. Wentzcovitch, *J. Phys.: Condens. Matter* **21**, 395502 (2009).
- ¹⁷J. P. Perdew, K. Burke, and M. Ernzerhof, *Phys. Rev. Lett.* **77**, 3865 (1996).
- ¹⁸S. M. Blinder, *Am. J. Phys.* **33**, 431 (1965).
- ¹⁹S. Hull and D. A. Keen, *Phys. Rev. B* **50**, 5868 (1994).
- ²⁰B. Amrani, T. Benmessabih, M. Tahiri, I. Chiboub, S. Hiadsi, and F. Hamdache, *Phys. B* **381**, 179 (2006).
- ²¹D. Huang, Y.-J. Zhao, S. Li, C.-S. Li, J.-J. Nie, X.-H. Cai, and C.-M. Yao, *J. Phys. D: Appl. Phys.* **45**, 145102 (2012).
- ²²M. Cardona, *Phys. Rev.* **129**, 69 (1963).
- ²³J. P. Perdew, *Int. J. Quantum Chem.* **28**, 497 (1985).
- ²⁴M. J. van Setten, M. Giantomassi, E. Bousquet, M. J. Verstraete, D. R. Hamann, X. Gonze, and G.-M. Rignanese, *Comput. Phys. Commun.* **226**, 39 (2018).
- ²⁵K. Shindo, A. Morita, and H. Kamimura, *J. Phys. Soc. Jpn.* **20**, 2054 (1965).
- ²⁶B. Prevot, B. Hennion, and B. Dorner, *J. Phys. C: Solid State Phys.* **10**, 3999 (1977).
- ²⁷S. Hoshino, Y. Fujii, J. Harada, and J. D. Axe, *J. Phys. Soc. Jpn.* **41**, 965 (1976).
- ²⁸B. Hennion, F. Moussa, B. Prevot, C. Carabatos, and C. Schawb, *Phys. Rev. Lett.* **28**, 964 (1972).
- ²⁹Y. Ma, J. S. Tse, and D. D. Klug, *Phys. Rev. B* **69**, 064102 (2004).
- ³⁰L. Börnstein, in *Numerical Data and Functional Relationships in Science and Technology, New Series, Group III*, edited by O. Madelung (Springer, Berlin, 1987), Vol. 22.
- ³¹I. P. Kaminow and E. H. Turner, *Phys. Rev. B* **5**, 1564 (1972).
- ³²M. Seifert, M. Kawashima, C. Rödl, and S. Botti, *J. Mater. Chem. C* **9**, 11284 (2021).
- ³³R. C. Hanson, J. R. Hallberg, and C. Schwab, *Appl. Phys. Lett.* **21**, 490 (1972).
- ³⁴Y. Li, J. Sun, and D. J. Singh, *Phys. Rev. Mater.* **2**, 035003 (2018).
- ³⁵F. Giustino, M. L. Cohen, and S. G. Louie, *Phys. Rev. B* **76**, 165108 (2007).
- ³⁶J. Noffsinger, F. Giustino, B. D. Malone, C.-H. Park, S. G. Louie, and M. L. Cohen, *Comput. Phys. Commun.* **181**, 2140 (2010).
- ³⁷N. Marzari and D. Vanderbilt, *Phys. Rev. B* **56**, 12847 (1997).
- ³⁸P. Yu and M. Cardona, *Fundamentals of Semiconductors: Physics and Materials Properties* (Springer Science & Business Media, 2010).
- ³⁹C. Jacoboni, *Theory of Electron Transport in Semiconductors: A Pathway from Elementary Physics to Nonequilibrium Green Functions* (Springer Science & Business Media, 2010), Vol. 165.
- ⁴⁰J. Ma, A. S. Nissimagoudar, and W. Li, *Phys. Rev. B* **97**, 045201 (2018).

- ⁴¹J. Bardeen and W. Shockley, *Phys. Rev.* **80**, 72 (1950).
- ⁴²Z. Li, P. Graziosi, and N. Neophytou, *Phys. Rev. B* **104**, 195201 (2021).
- ⁴³K. Seeger, *Semiconductor Physics: An Introduction* (Springer-Verlag, Berlin, 2004).
- ⁴⁴P. Y. Yu and M. Cardona, *Fundamentals of Semiconductors* (Springer, Berlin, 2005).
- ⁴⁵M. Costato, and L. Reggiani, *J. Phys. C: Solid State Phys.* **5**, 159 (1972).
- ⁴⁶W. Fawcett, A. D. Boardman, and S. Swain, *J. Phys. Chem. Solids* **31**, 1963 (1970).
- ⁴⁷B. Hönerlage, C. Klingshirn, and J. B. Grun, *Phys. Status Solidi B* **78**, 599 (1976).
- ⁴⁸C. I. Yu, T. Goto, and M. Ueta, *J. Phys. Soc. Jpn.* **34**, 693 (1973).
- ⁴⁹M. Ferhat, A. Zaoui, M. Certier, J. P. Dufour, and B. Khelifa, *Mater. Sci. Eng. B* **39**, 95 (1996).
- ⁵⁰J. Dewey and M. A. Osman, *J. Appl. Phys.* **74**, 3219 (1993).
- ⁵¹S. Rodríguez-Bolívar, F. M. Gómez-Campos, and J. E. Carceller, *Semicond. Sci. Technol.* **20**, 16 (2004).
- ⁵²G. Dresselhaus, A. F. Kip, and C. Kittel, *Phys. Rev.* **98**, 368 (1955).
- ⁵³S. Rodríguez-Bolívar, F. M. Gómez-Campos, F. Gámiz, and J. E. Carceller, *J. Appl. Phys.* **97**, 013702 (2005).
- ⁵⁴C. dos Soares, G. I. Wirth, A. Rossetto, and D. Vasileska, *J. Integr. Circuits Syst.* **16**, 1 (2021).
- ⁵⁵D. Vasileska and S. M. Goodnick, see <https://nanohub.org/resources/9109> for "Bulk Monte Carlo: Implementation details and source codes download" (2010).
- ⁵⁶C. Jacoboni and L. Reggiani, *Rev. Mod. Phys.* **55**, 645 (1983).
- ⁵⁷K. Hess, *Monte Carlo Device Simulation: Full Band and Beyond* (Kluwer Academic, Boston, 1991).
- ⁵⁸M. Lundstron, *Fundamentals of Carrier Transport* (Cambridge University Press, Cambridge, 2000).
- ⁵⁹X. Li, J. T. Mullen, Z. Jin, K. M. Borysenko, M. Buongiorno Nardelli, and K. W. Kim, *Phys. Rev. B* **87**, 115418 (2013).
- ⁶⁰Z. Jin, X. Li, J. T. Mullen, and K. W. Kim, *Phys. Rev. B* **90**, 045422 (2014).
- ⁶¹P. J. Briggs, A. B. Walker, and D. C. Herbert, *Semicond. Sci. Technol.* **13**, 680 (1998).
- ⁶²B. E. Foutz, S. K. O'Leary, M. S. Shur, and L. F. Eastman, *J. Appl. Phys.* **85**, 7727 (1999).
- ⁶³K. Ghosh and U. Singiseti, *J. Appl. Phys.* **122**, 035702 (2017).
- ⁶⁴D. Chen, Y. Wang, Z. Lin, J. Huang, X. Chen, D. Pan, and F. Huang, *Cryst. Growth Des.* **10**, 2057 (2010).
- ⁶⁵M. Grundmann, F.-L. Schein, M. Lorenz, T. Böntgen, J. Lenzner, and H. von Wenckstern, *Phys. Status Solidi A* **210**, 1671 (2013).
- ⁶⁶C. Yang, M. Kneiß, F.-L. Schein, M. Lorenz, and M. Grundmann, *Sci. Rep.* **6**, 21937 (2016).
- ⁶⁷C. Yang, D. Souchay, M. Kneiß, M. Bogner, H. M. Wei, M. Lorenz, O. Oeckler, G. Benstetter, Y. Q. Fu, and M. Grundmann, *Nat. Commun.* **8**, 16076 (2017).
- ⁶⁸A. Liu, H. Zhu, M. Kim, J. Kim, and Y. Noh, *Adv. Sci.* **8**, 21000546 (2021).